Monthly Notices of the ROYAL ASTRONOMICAL SOCIETY

MNRAS **527,** 2279–2287 (2024) https://doi.org/10.1093/mnras/stad3140
Advance Access publication 2023 October 13

Collisional excitation of PO^+ by *para*-H_2: potential energy surface, scattering calculations, and astrophysical applications

F. Tonolo [1,2★] L. Bizzocchi [2★] V. M. Rivilla [3] F. Lique [4] M. Melosso [2] and C. Puzzarini [2]

[1] *Scuola Normale Superiore, Piazza dei Cavalieri 7, I-56126 Pisa, Italy*
[2] *Dipartimento di Chimica 'Giacomo Ciamician', Università di Bologna, Via F. Selmi 2, I-40126 Bologna, Italy*
[3] *Centro de Astrobiología (CAB), INTA-CSIC, Carretera de Ajalvir km 4, Torrejón de Ardoz, E-28850, Madrid, Spain*
[4] *Université de Rennes, CNRS, IPR (Institut de Physique de Rennes) – UMR 6251, F-35000 Rennes, France*

Accepted 2023 October 9. Received 2023 October 9; in original form 2023 August 11

ABSTRACT

We report the derivation of rate coefficients for the rotational (de-)excitation of PO^+ induced by collisions with H_2. The calculations were performed on a 4D potential energy surface, obtained on top of highly accurate *ab initio* energy points. Preliminary tests pointed out the low influence of the coupling between $j = 0$ and the higher rotational levels of H_2 on the cross-sections values, thus allowing to neglect the rotational structure of H_2. On this basis, state-to-state collisional rate coefficients were derived for temperatures ranging from 5 to 200 K. Radiative transfer calculations have been used to model the recent observation of PO^+ in the G+0.693–0.027 molecular cloud, in order to evaluate the possible impact of non-LTE models on the determination of its physical conditions. The derived column density was found to be approximately $\sim 3.7 \times 10^{11}$ cm^{-2}, which is 60% (a factor of ~ 1.7) smaller than the previously LTE-derived value. Extensive simulations show that PO^+ low-j rotational lines exhibit maser behaviour at densities between 10^4 and 10^6 cm^{-3}, thus highlighting the importance of a proper treatment of the molecular collisions to accurately model PO^+ emissions in the interstellar medium.

Key words: molecular data – molecular processes – scattering – ISM: abundances.

1 INTRODUCTION

The investigation of the cosmic abundance and distribution of phosphorus (P) in space deserves a special attention as it is considered a biogenic element together with carbon, hydrogen, oxygen, nitrogen, and sulphur (CHONPS; Rivilla et al. 2016; Öberg & Bergin 2021; Bergner et al. 2022). In particular, P has a pivotal importance for 'abiogenesis', namely, the formation of prebiotic species from abiotic systems (Pearce et al. 2017). It is indeed a key ingredient for the composition of many biomolecules, especially when bonded with O atoms in the form of phosphate (PO_4^{3-}). For this reason, P is an ubiquitous element in our planet and its abundance in living organisms is relatively high (Fagerbakke, Heldal & Norland 1996). Outside Earth, P-bearing compounds have been found in a variety of environments, from the planetary atmospheres of Jupiter and Saturn (Bregman, Lester & Rank 1975; Ridgway, Wallace & Smith 1976) to meteorites (Pasek & Lauretta 2005; Schwartz 2006), as well as in the 67P/Churyumov–Gerasimenko comet (Altwegg et al. 2016; Rivilla et al. 2020) and in circumstellar envelopes of evolved stars (Agúndez, Cernicharo & Guélin 2007; Tenenbaum, Woolf & Ziurys 2007; Halfen, Clouthier & Ziurys 2008; Agúndez et al. 2014; Rivilla et al. 2020). Recently, P has also been found in Enceladus's ocean in the form of orthophosphates, opening a new window on the origin of life under the frozen surfaces of Jupiter's moons (Postberg et al. 2023).

All this contrasts with its actual, limited distribution in the interstellar medium (ISM), where only a few P-bearing molecules have been identified (see Rivilla et al. 2022 and references therein), despite numerous searches (e.g. Chantzos et al. 2020). Such elusiveness may be due to the high sublimation temperature of atomic P, which leads to a strong depletion of this element onto interstellar grains (Lebouteiller & Ferlet 2005). The first P-bearing species detected in the ISM were PN (Turner & Bally 1987; Ziurys 1987) and the CP radical (Guélin et al. 1990), whereas the possible precursor of this latter, HCP, was observed almost 20 yr later (Agúndez, Cernicharo & Guélin 2007). From 2007 to date, few other molecules have been observed, namely PO (Lefloch et al. 2016; Rivilla et al. 2016, 2018; Bergner et al. 2019), C_2P (Halfen, Clouthier & Ziurys 2008), PH_3 (Agúndez et al. 2014) and, very recently, PO^+ (Rivilla et al. 2022).

Besides the paucity of observational data, only few studies on P-reactivity (Viana et al. 2009; Alessandrini, Tonolo & Puzzarini 2021; de la Concepción et al. 2021; Baptista & De Almeida 2023) and chemical modelling (Fontani et al. 2016; Lefloch et al. 2016; Rivilla et al. 2016, 2022; Jiménez-Serra et al. 2018; Chantzos et al. 2020) are present in the literature, thus making the understanding of the P chemistry in the ISM far from being satisfactory. Overcoming this lack of information requires a major astrochemical effort, and the first step is achieving new detections of P-bearing species complemented by a reliable determination of their abundances. This latter aspect calls for extra caution for environments where local thermodynamic

★ E-mail: francesca.tonolo@sns.it (FT); luca.bizzocchi@unibo.it (LB)

equilibrium (LTE) conditions may not be fulfilled, and radiative transfer calculations should be undertaken. Under such conditions, the estimate of molecular abundances from spectral lines requires the knowledge of the collisional rate coefficients of the target species with the most abundant perturbing gas, i.e. molecular hydrogen (H_2), with He sometimes being considered as approximation for *para*-H_2 ($j = 0$) (Roueff & Lique 2013).

An interesting case is given by the recent detection of PO^+ in the molecular cloud G+0.693–0.027 (Rivilla et al. 2022), located in the SgrB2 region of the centre of the Galaxy, where other P-bearing species where previously detected (Rivilla et al. 2018). This source is characterized by a H_2 gas density of several 1×10^4 cm^{-3} (Zeng et al. 2020). Due to this relatively low density, the LTE conditions are not achieved, and hence the energy levels of the molecules are not thermalized at the kinetic temperature of the cloud (~ 150 K; Zeng et al. 2018). This motivates the need of collisional rate coefficients to properly describe the molecular excitation of PO^+. Recently, Chahal & Dhilip Kumar (2023) investigated the collisional behaviour of PO^+ with He and provided the first set of collisional coefficients for non-LTE modelling of the abundance of PO^+ in the ISM. However, for molecular hydrides and ions, He does not represent a suitable template for collisions with H_2 (Roueff & Lique 2013).

In order to provide collisional data that meet the astrophysical needs, we investigated the collision of PO^+ with *para*-H_2. These new data allowed us to test the reliability of the LTE approximation and to refine the column density value of PO^+ obtained from the observations of the G+0.693–0.027 molecular cloud (Rivilla et al. 2022). This paper is organized as follows: Section 2 provides the computational details – for both the calculation of the interaction potential (Section 2.1) and dynamics (Section 2.2) – to derive the collisional rate coefficients. Section 3 assesses the impact of the collisional data on the modelling of the column density of PO^+ in G+0.693–0.027 cloud. Finally, in Section 4, the main outcomes of this investigation are presented.

2 COMPUTATIONAL DETAILS

The starting point to derive the collisional coefficients of a molecular system is the calculation of the interaction potential between the two colliding partners, in this case PO^+ and H_2. This serves as a basis to solve the nuclear Schrödinger equation, which describes the quantum scattering problem, thus providing the S matrix that contains all collisional information on the target system. Both of these steps, detailed in the following two subsections, require extensive calculations that need to balance accuracy, suitability for physical applications, and computational efficiency.

2.1 Potential energy surface

The interaction between PO^+ and H_2 has been described by a set of four Jacobi coordinates, as depicted in Fig. 1. These correspond to (i) the distance R between the centre of mass of PO^+ and that of H_2, (ii) the angle θ between the molecular axis of PO^+ and the vector **R**, and two angles, (iii) θ', and (iv) ϕ, defining the orientation of H_2 in and out the plane formed by PO^+ and vector **R**.

The interaction energies between the two collisional partners have been computed over a $\{R, \theta, \theta', \text{and } \phi\}$ grid, purposely chosen to accurately sample the anisotropy of the system. Moreover, PO^+ and H_2 were considered as rigid bodies, as we expect all the vibrational channels to be closed at the typical ISM physical conditions (Stoecklin et al. 2013). The PO^+ bond length was held fixed at its experimental equilibrium value (Petrmichl, Peterson & Woods 1991): $r(PO^+) = 1.4250$ Å. For H_2, we adopted the bond length corresponding to the averaged value over its ground vibrational state: $r_0(H_2) = 0.7667$ Å (Jankowski & Szalewicz 1998).

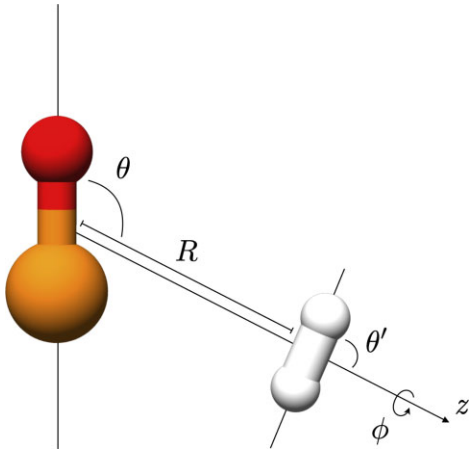

Figure 1. Jacobi internal coordinates of the $PO^+ - H_2$ collisional system.

The electronic energy for each point of the $\{R, \theta, \theta', \text{and } \phi\}$ grid has been computed using the explicitly correlated CCSD(T)-F12a method (Adler, Knizia & Werner 2007; Peterson, Adler & Werner 2008; Knizia, Adler & Werner 2009), where the acronym stands for coupled cluster singles, doubles, and a perturbative treatment of triple excitations (Raghavachari et al. 1989), in conjuction with the aug-cc-pVQZ basis set augmented by an additional d function on second-row atoms (Woon & Dunning 1993; Dunning, Peterson & Wilson 2001). Hereafter, this level of theory is denoted as CCSD(T)-F12a/aug-cc-pV(Q+d)Z. The aug-cc-pV(Q+d)Z basis set has been chosen because the inclusion of diffuse functions (denoted by the aug- prefix) has proven to yield better performances in computing the electronic energies of charged systems, in which the electron density extends relatively far from the global maximum (Kendall, Dunning & Harrison 1992; Tonolo et al. 2021). For all the calculations, the MOLPRO suite of programs[1] (Werner et al. 2012) has been employed.

The interaction energies were computed as the difference between the energy of the molecular complex (E_{AB}) and the sum of the energies of the two fragments (E_A and E_B). All the terms have also been corrected for the basis set superposition error (BSSE) by means of the counterpoise (CP; Boys & Bernardi 1970) correction scheme:

$$\Delta E_{CP} = \left(E_A^{AB} - E_A^{A}\right) + \left(E_B^{AB} - E_B^{B}\right) . \quad (1)$$

Here, E_X^{AB} is the energy of the monomer calculated with the same basis set used for the cluster and E_X^X is the energy of the monomer computed with its own basis set (X = A, B).

To achieve an accurate characterization of the potential energy surface (PES) of the PO^+–H_2 system, the coordinates of the *ab initio* points were chosen in order to build up a dense mesh near the most anisotropic parts of the potential, whereas a coarser grid was adopted in regions where the energy mildly depends on the system geometry. In order to further reduce the computational cost, we considered only five orientations of H_2 with respect to PO^+, described by the $\{\theta', \phi\}$ coordinates. This approximation has been found appropriate for similar systems (e.g. HCO^+/H_2; see Tonolo et al. 2022) since the dependence of the potential on the orientation of H_2 is very weak.

[1] https://www.molpro.net.

This statement deserves a more detailed note. In a two rigid rotor system, the interaction potential can be retrieved from *ab initio* points by fitting them as an expansion over angular functions of the following form (Green 1975; Wernli et al. 2007a, b):

$$V\left(R,\theta,\theta',\phi\right)=\sum_{l_1 l_2 \mu} v_{l_1 l_2 \mu}(R) s_{l_1 l_2 \mu}\left(\theta,\theta',\phi\right) . \quad (2)$$

Here, $v_{l_1 l_2 \mu}(R)$ are the radial coefficients and the l_1, l_2, and μ are indices associated with the rotational angular moments of PO$^+$(j_1), H_2(j_2) and their vector sum, respectively. $s_{l_1 l_2 \mu}$ are the angular coefficients, defined as products of spherical harmonics, $Y_{l_i m}(\theta',\phi)$, and Clebsch–Gordan vector-coupling coefficients (the reader is referred to Green 1975; Brown, Brown & Carrington 2003; Edmonds 2016 for further details). If we assume $l_2 \leq 2$, there are only four spherical harmonic functions that shape the dependence of the potential on each set of $\{\theta',\phi\}$. Hence, the choice of five orientations of H_2 with respect to PO$^+$ not only suffices to describe the corresponding angular dependence of the potential, but also provides an overdetermined system to test the accuracy of the $l_2 \leq 2$ truncation (see for details, Wernli 2006; Tonolo et al. 2022).

The five orientations chosen (x, y, z, a, and b) are the same as those used by Wernli (2006) and Tonolo et al. (2022) for the HC_3N/H_2 and HCO^+/H_2 systems and are depicted in the insets of Fig. 2. For each of them, 650 interaction energies were computed, spanning through 25 θ angle values equally spaced from 0 to 180 degrees and 26 R distances, varying between 2 and 12 Å , and with a denser mesh between 2.6 and 3.6 Å. Each set of $\{\theta',\phi\}$ energies has been subsequently expressed as an expansion over P_λ Legendre polynomials within the following expression (Lique & Faure 2019):

$$V\left(R,\theta\right)=\sum_{\lambda} v_\lambda(R) P_\lambda\left(\cos\theta\right) . \quad (3)$$

The $v_\lambda(R)$ radial coefficients have been fitted to a functional form which takes into account the sizable contribution due to induction interactions of the PO$^+$ ion:

$$v_\lambda(R)=\mathrm{e}^{-a_1^\lambda R}\left(a_2^\lambda+a_3^\lambda R+a_4^\lambda R^2+a_5^\lambda R^3\right) - \frac{1}{2}\left[1+\tanh\left(R/R_{\mathrm{ref}}\right)\right]\left(\frac{C_4^\lambda}{R^4}+\frac{C_6^\lambda}{R^6}+\frac{C_8^\lambda}{R^8}+\frac{C_{10}^\lambda}{R^{10}}\right), \quad (4)$$

where a_n^λ label the coefficients of the short-range region ($0 < R < R_{\mathrm{ref}}$) and C_n^λ the R^{-n} terms in the long-range extrapolated domain ($R > R_{\mathrm{ref}}$). For each angular dependency block, all coefficients and the R_{ref} value were optimized within the fit.

For each orientation, the fitted points resulted in good agreement with the corresponding *ab initio* computed ones, with deviations on average within 1% over the entire grid. The energy plots corresponding to the chosen H_2 orientations are shown in Fig. 2. It is apparent the weak anisotropy of the potential with respect to the $\{\theta',\phi\}$ coordinates, thus validating the choice of truncating the potential to the $l_2 \leq 2$ terms. For each orientation, the potential exhibits a minimum at $R \sim 2.8$ Å and $\theta \sim 112.5$ degrees, i.e. with the H_2 slightly leaning towards the phosphorous side of PO$^+$ (see Fig. 1, where R and θ have been purposely set to depict the minimum of the potential).

The 4D potential of the system was finally retrieved by introducing a functional dependence on the four spherical harmonics (for the explicit dependence on the $\{\theta',\phi\}$ coordinates the reader is referred to Equation (6) in Tonolo et al. 2022):

$$\begin{aligned} V\left(R,\theta,\theta',\phi\right) &= 2\sqrt{\pi}\, V_{\mathrm{av}}(R,\theta)\, Y_{00}(\theta',\phi)+ \\ &+2\sqrt{\frac{\pi}{5}}\left[V(R,\theta,z)-V_{\mathrm{av}}(R,\theta)\right] Y_{20}(\theta',\phi)+ \\ &+\sqrt{\frac{3\pi}{10}}\left[V(R,\theta,a)-V(R,\theta,b)\right]\left[Y_{2-1}(\theta',\phi)-Y_{21}(\theta',\phi)\right]+ \\ &+\sqrt{\frac{2\pi}{15}}\left[V(R,\theta,x)-V(R,\theta,y)\right]\left[Y_{2-2}(\theta',\phi)+Y_{22}(\theta',\phi)\right], \end{aligned} \quad (5)$$

where $V_{\mathrm{av}}(R,\theta)$ is the potential averaged over the five $\{\theta',\phi\}$ orientations:

$$V_{\mathrm{av}}(R,\theta)=\frac{1}{7}\left[2\left(V(R,\theta,a)+V(R,\theta,b)\right)+ +\left(V(R,\theta,x)+V(R,\theta,y)+V(R,\theta,z)\right)\right], \quad (6)$$

for which a contour plot representation is shown in Fig. 3.

The behaviour of our potential is perfectly consistent with the trend of that computed by Chahal & Dhilip Kumar (2023) for the interaction between PO$^+$ and He, although – as expected – the magnitude of the interaction is almost seven times higher in terms of energy: for the $\{\theta'=90,\phi=0\}$ orientation with H_2, corresponding to the global (and unique) minimum of the potential, the energy is 1234.12 cm^{-1}, while for the interaction with He the minimum is located at 181.97 cm^{-1}.

2.2 Scattering calculations

The second step in the derivation of the PO$^+$–H_2 collisional rate coefficients is to perform dynamics calculations on top of the interaction potential. In this work, full quantum close-coupling (CC) calculations were carried out by employing the MOLSCAT program[2] (Hutson & Green 1994). Since our objective is to derive reliable state-to-state rate coefficients up to 200 K, we thus targeted a total energy interval from 2 to 1200 cm^{-1}. Because of the irregular trends exhibited by the cross-sections at low kinetic energies, we sampled with very fine steps (0.2 cm^{-1}) the interval 2–50 cm^{-1}, which have been then gradually increased up to 50 cm^{-1} of step size above 500 cm^{-1}.

The angular part of the nuclear Schrödinger equation has been solved, and the radial dependence has then been modelled by numerical propagation. The employed propagator, also called LDMD/AIRY (Alexander 1984; Manolopoulos 1986; Alexander & Manolopoulos 1987), is an hybrid function that combines the Manolopoulos diabatic modified log-derivative (LDMD) propagator in the short range of R with the Alexander–Manolopoulos Airy (AIRY) one for long R distances. The former, indeed, uses a narrower propagation step when the energy gradient is higher, thus providing a good balance between stability and efficiency. The latter instead is particularly efficient at higher values of R, where a broader range needs to be covered, since it accounts for looser propagation steps. We started the integration at $R = 1.8$ Å and the switch point between the two propagators and the long range limit value were adjusted to ensure convergence within 2% for the inelastic cross-sections in the considered energy range.

The rotational basis adopted for PO$^+$ included the first 32 rotational levels in the low energy range (2–50 cm^{-1}), extended up to $j = 50$ in the high-energy end of the scattering calculations (1200 cm^{-1}). The choice of the rotational basis of H_2 requires some extra remarks. The 4D potential defined above constitutes the best representation of the system as it also includes for the calculation of

[2]https://github.com/molscat/molscat.

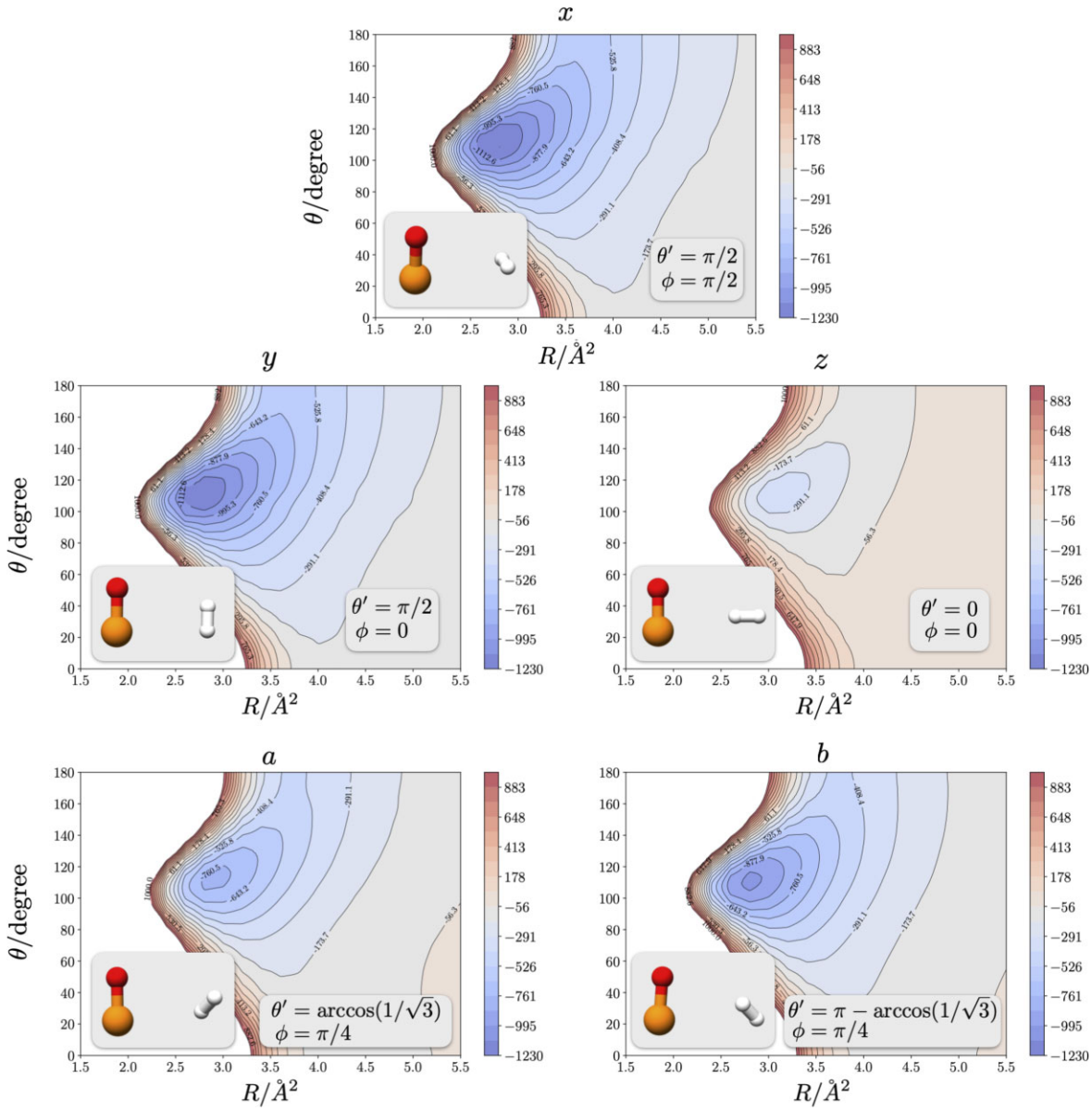

Figure 2. Contour plots of the PO^+–H_2 interaction PES for five different orientations of H_2.

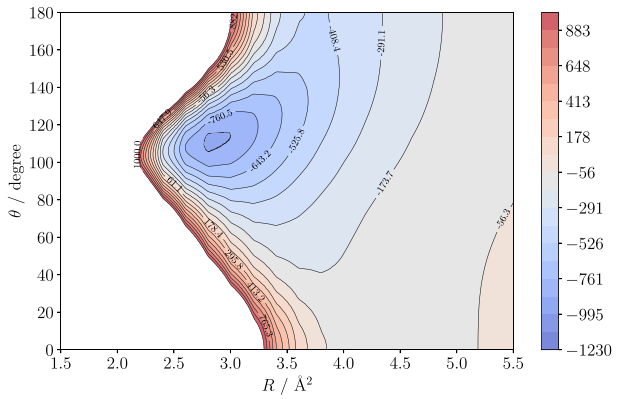

Figure 3. Contour plots of the averaged potential of PO^+–H_2 over the five $\{\theta', \phi\}$ orientations (see Equation 6).

each cross-section the influence of the $j > 0$ rotational states of H_2. This, however, implies a major computational effort.

The impact of the coupling between $j = 0$ and $j > 0$ rotational states of H_2 can be evaluated by performing a few comparative calculations of cross-sections at 150 cm^{-1} using both the global 4D potential and the averaged 2D one, this latter being obtained from Equations (3) and (6) of the previous section. The use of the 2D averaged potential, also known as the spherical approximation, is equivalent to treat the H_2 projectile as a structureless species, i.e. behaving as a rotating sphere (*para*-H_2 with $j = 0$). Such approximation has already been found to be successful especially with ions and it significantly reduces the cost of the collision dynamics calculations (Spielfiedel et al. 2015; Balança et al. 2020; Cabrera-González, Páez-Hernández & Denis-Alpizar 2020; Tonolo et al. 2022). In this case, the comparison between the 2D potential and the full 4D potential, in which the coupling with $j = 2$ rotational level was included, showed a mean average relative deviation of ∼ 7.0% and a maximum discrepancy of 14.7%. These deviations on the cross-sections, reported in Table 1,

Table 1. Computed cross-sections at $E = 150\,\mathrm{cm}^{-1}$ for $PO^+ - H_2(j = 0)$ collisions obtained from the 2D spherically averaged potential and with the full 4D potential, which includes the coupling with $j = 2$ rotational level of H_2. The comparison of the cross-sections accounting for collisions between *para*-H_2 ($j = 0$) and *ortho*-H_2 ($j = 1$) is also reported.

$j' \rightarrow j$	Cross-sections/Å^2			% deviation	
	$j = 0$		$j = 1$	2D/4D	*o-/p-*
	2D	4D			
$1 \rightarrow 0$	33.10	30.46	33.84	− 8.68	2.19
$2 \rightarrow 0$	17.43	19.16	20.46	9.02	14.81
$3 \rightarrow 0$	9.32	8.48	10.88	− 9.88	14.35
$4 \rightarrow 0$	12.64	11.89	14.39	− 6.29	12.17
$2 \rightarrow 1$	26.61	24.55	29.11	− 8.42	8.57
$3 \rightarrow 1$	16.84	15.16	19.70	− 11.08	14.52
$4 \rightarrow 1$	11.75	12.82	13.16	8.38	10.72
$3 \rightarrow 2$	26.06	30.57	27.96	14.73	6.79
$4 \rightarrow 2$	15.67	14.23	18.19	− 10.14	13.87
$4 \rightarrow 3$	27.30	28.84	31.06	5.32	12.10
Average absolute % deviation				7.30	19.02

fall within the desired level of accuracy for astrophysical applications and justify the use of the spherical average potential approximation over the entire energy grid. Given the physical conditions of the region where PO^+ was observed, where – despite the low densities – the kinetic temperature is about 150 K, collisions with *ortho*-H_2 should be considered too. For this reason, in Table 1, a comparison of the cross-sections obtained for collisions with *para*-$H_2(j = 0)$ and *ortho*-$H_2(j = 1)$ is also provided. Here, the mean average relative deviation is $\sim 19\%$, with a maximum discrepancy of 48.24%. Given such differences, we do not expect large discrepancies between the rate coefficients for collisions with *ortho*- and *para*-H_2, thus justifying the use of only *para*-$H_2(j = 0)$ in the rotational basis of our scattering calculations. This assumption is also in accordance with the results reported for other ions, e.g. Kłos & Lique (2011), Walker et al. (2017), Dagdigian (2019), Desrousseaux et al. (2019), and Lara-Moreno, Stoecklin & Halvick (2019).

The final calculations were, thus performed using the 2D averaged potential, and the maximum value of the total angular momentum (J) was chosen to allow for convergence of the inelastic cross-sections within 0.005 Å^2. The reduced mass (μ) of the collisional system was set to 1.9327 u, while the rotational energies of the two colliders were calculated from their equilibrium rotational and quartic centrifugal distortion constants. For PO^+, $B_e = 0.787\,\mathrm{cm}^{-1}$ and $D_e = 9.786 \times 10^{-7}\,\mathrm{cm}^{-1}$ were adopted (Petrmichl, Peterson & Woods 1991). For H_2 molecule, the data given by Huber et al. (1979) were employed: $B_e = 60.853\,\mathrm{cm}^{-1}$ and $D_e = 4.71 \times 10^{-2}\,\mathrm{cm}^{-1}$.

From the derived S matrix elements, the cross-sections ($\sigma(E_c)$) from an initial j to a final j' state of PO^+ at a given collision energy (E_c) can be retrieved. The energy dependence of some of them, involving the first rotational states of PO^+, as a function of E_c, is illustrated in Fig. 4. Starting from inelastic ($j' \neq j$) cross-sections, the de-excitation rate coefficients, $k_{j \rightarrow j'}(T)$, are straightforwardly derived by thermal averaging over the E_c:

$$k_{j \rightarrow j'}(T) = \left(\frac{8}{\pi \mu k^3 T^3}\right)^{1/2} \times \int_0^\infty \sigma_{j \rightarrow j'}(E_c)\, E_c \exp(-E_c/kT)\, \mathrm{d}E_c, \quad (7)$$

where k is the Boltzmann constant. We computed the (de)-excitation rate coefficients for the 20 lowest rotational levels of PO^+ in the 5−200 K temperature range. The complete set of them will be made

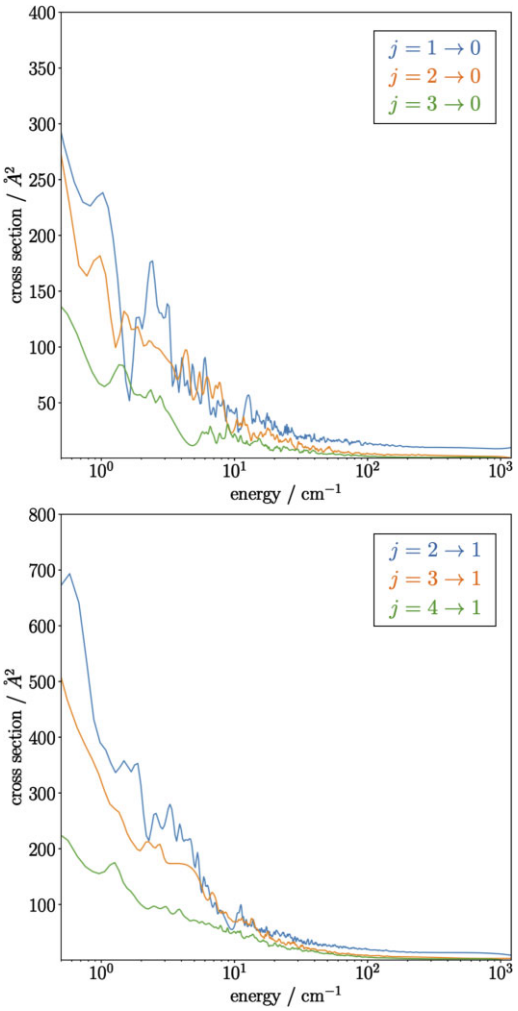

Figure 4. Variation of some rotational de-excitation cross-sections in the 2–1200 cm^{-1} energy range.

available through the LAMDA (Schöier et al. 2010; van der Tak et al. 2020) and BASECOL (Dubernet et al. 2013) data bases. The plots in Fig. 5 illustrate the temperature dependence of selected coefficients for which $j' \rightarrow 0$, $j' \rightarrow 1$ (upper plot) and $\Delta j = 1$ (bottom plot). A propensity towards transitions involving $\Delta j = 1$ clearly stands out, while it decreases with the increment of Δj. In addition, inelastic rate coefficients exhibit a propensity towards transitions involving j levels with the highest multiplicity although, at low temperatures ($T < 50\,K$), this preference may reverse. This pattern is in accordance with the one observed for the isoelectronic species NO^+ with *para*-H_2 (Cabrera-González, Páez-Hernández & Denis-Alpizar 2020). This agreement is also reflected in the comparison of the values of the rate coefficients for the two species. The recent collisional study on the PO^+/He system (Chahal & Dhilip Kumar 2023), moreover, provides us a basis to test the suitability of using He to simulate the behaviour of *para*-H_2. The mass-scaled rate coefficients Schöier et al. (2005) for the collision of PO^+ with He, however, resulted to highly underestimate the values obtained with H_2, leading to discrepancies up to one order of magnitude in several cases. In addition, the two sets of rate coefficients exhibit different behaviours at temperatures below 50 K, including also divergent propensity rules. Since these discrepancies are particularly evident under the typical ISM conditions, only collisional data with H_2 provide the

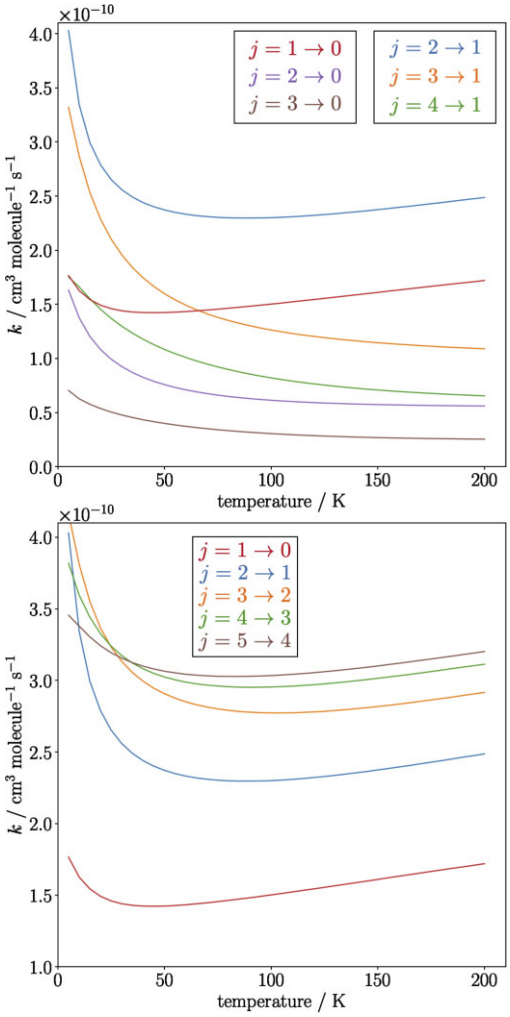

Figure 5. Variation of some rotational de-excitation rate coefficients as a function of T_{kin}.

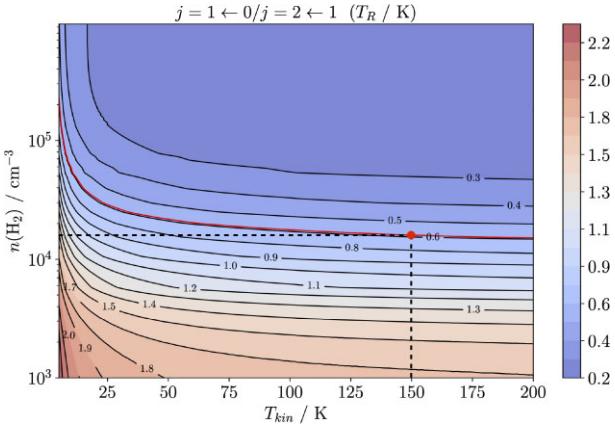

Figure 6. Contour plot showing the variation of the intensities ratio $j = 1{-}0/j = 2{-}1$ with respect to the change of $T_{\rm kin}$ (x axis) and $n(\rm H_2)$ (y-axis). The isocurve of the intensity ratio observed by Rivilla et al. (2022) is highlighted in red.

most reliable means for astrophysical applications. Indeed, it is well established (Yazidi, Ben Abdallah & Lique 2014; Bop 2019; Denis-Alpizar & Rubayo-Soneira 2019; Cabrera-González, Páez-Hernández & Denis-Alpizar 2020) that the inaccuracy of He as a template of the $\rm H_2$ perturber is particularly pronounced in the case of ions because of the different behaviour of the long range part of the potential for the ion-He and ion-$\rm H_2$ interactions.

3 ASTROPHYSICAL APPLICATIONS

Our new collisional coefficients provide a good basis to test the suitability of the LTE approximation to model the transitions detected by Rivilla et al. (2022) in the G+0.693–0.027 molecular cloud. Due to the relatively low density of this source (several 1×10^4 cm^{-3}; Zeng et al. 2020), the energy levels of the molecules are not thermalized at the kinetic temperature of the cloud ($\sim$ 150 K; Zeng et al. 2018), but they reach a 'quasi-thermalization' at an excitation temperature ($T_{\rm ex}$) that is significantly lower than $T_{\rm kin}$ (see detailed explaination of this effect in Goldsmith & Langer 1999). In absence of collisional data, LTE approach is hence used, giving typical $T_{\rm ex}$ in the range of 5–20 K (see Zeng et al. (2018)). The spectral survey in Rivilla et al. (2022) covered four different rotational transitions of $\rm PO^+$, though, only the $j = 1{-}0$ and $j = 2{-}1$ ones appear free from contamination by other species. This implies the system to have only two degrees of freedom for the rotational population modelling, thus the retrieved physical parameters are to be viewed with some caution.

We performed radiative transfer calculations using the RADEX code[3] (Van der Tak et al. 2007). Since the structure and dynamics of G+0.693–0.027 cloud is not well-constrained, the source geometry was approximated to a static sphere of uniform density. We also assumed $T_{\rm CMB} = 2.73$ K as background temperature, while the line width was set at 18 km s^{-1}, in accordance with observations (Rivilla et al. 2022). State-to-state collisional coefficients involving the first twenty rotational levels of $\rm PO^+$, in the temperature range from 5 to 200 K, and a $\rm PO^+$ dipole moment of 3.13 debye (Rivilla et al. 2022) have been employed for the calculation of the Einstein A coefficients of the corresponding $(j + 1){-}j$ radiative transitions.

At first, we performed a preliminary test of the variation of the $(j = 1{-}0)/(j = 2{-}1)$ intensity ratio as a function of both the kinetic temperature ($T_{\rm kin}$) and the density of hydrogen ($n(\rm H_2)$). The result is illustrated in Fig. 6, where the isocontours corresponding to the observed intensity ratio (0.64) have been marked in red. It is obvious that the constraint of the $T_{\rm kin}$ on $n(\rm H_2)$ is very weak, particularly when $T_{\rm kin} > 100$ K. Such a mild dependence allows us to retrieve a reliable estimate of the gas density of G+0.693–0.027, irrespective of the possible inaccuracies of $T_{\rm kin} \sim 150$ K. In fact, from the observed intensity ratio we obtain $n(\rm H_2) \sim 1.5 \times 10^4$ cm^{-3}, in good agreement with the value previously estimated by Zeng et al. (2020) of $\sim 1 \times 10^4$ cm^{-3}.

Going into the analysis of the single transitions, we plot in Fig. 7 the line intensity trends at 150 K as a function of $n(\rm H_2)$ and the column density (N). Again, the isocontours corresponding to the observed results, i.e. 7 mK for $j = 1{-}0$ and 11 mK for $j = 2{-}1$, are highlighted in red. Both plots substantially agree in indicating that, for $n(\rm H_2)$ $\sim 1.5 \times 10^4$ cm^{-3}, the observed line intensities imply a $\rm PO^+$ column density of $\sim 3.7 \times 10^{11}$ cm^{-2}, a value which is $\sim$60% (a factor of $\sim$1.7) lower than that retrieved from LTE assumption (Rivilla et al. 2022). The reason of this slight difference is that the LTE model tends to underestimate the population of the higher-energy levels, therefore requiring a higher column density to reproduce the observed intensities. The decrease in the actual value of the column density

[3] https://home.strw.leidenuniv.nl/~moldata/radex.html.

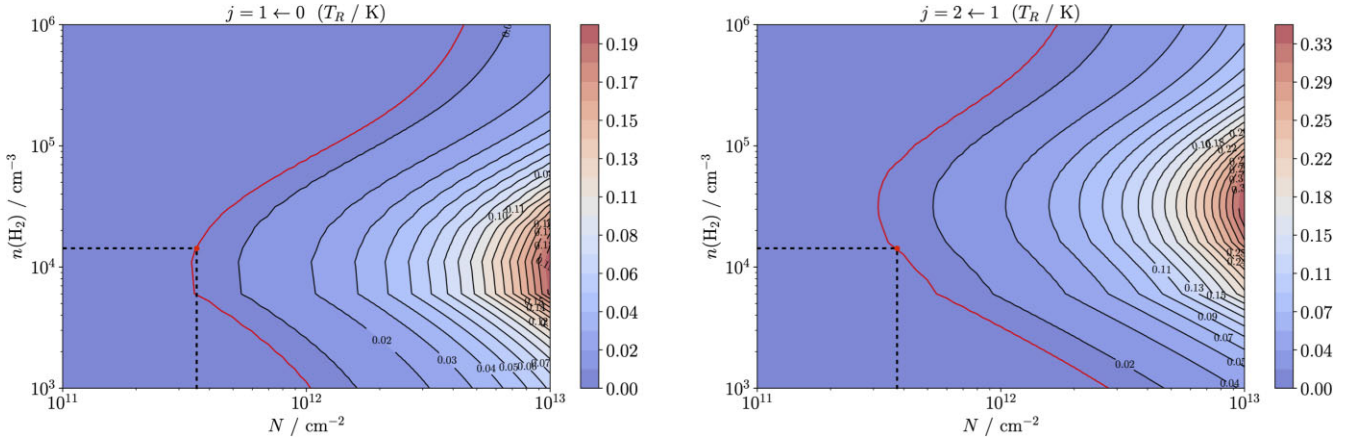

Figure 7. Contour plot showing the variation of the $j = 1-0$ and $j = 2-1$ intensities with respect to the change of the column density (x axis) and $n(H_2)$ (y-axis). The isocurves of the two intensities observed by Rivilla et al. (2022) are highlighted in red.

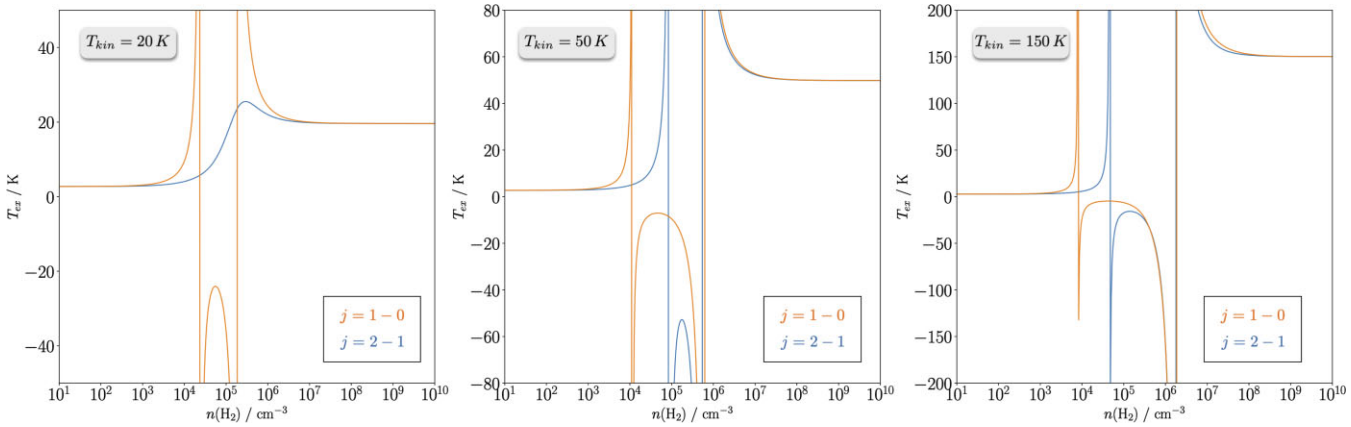

Figure 8. Variation of excitation temperature as a function of $n(H_2)$ for the first two transitions of PO$^+$ at $T_{kin} = 20, 50$, and 150 K.

of PO$^+$ is also reflected in a diminution of the N(PO$^+$)/N(PO) ratio derived by Rivilla et al. (2022), which becomes ~ 0.072. This leads to a reduction in the PO ionization rate previously predicted, which nevertheless remains predominant with respect to those retrieved for NO and SO.

In any case, the outcome of our analysis is that the LTE approximation to model low-j lines of PO$^+$ provides reasonable results when applied to the physical conditions of G+0.693–0.027. As has already been found (e.g. see discussion in Colzi et al. 2022), indeed, in G+0.693–0.027 the 'quasi-thermalization' condition is often fulfilled, with the distribution of the population among the levels being adequately described by only one T_{ex}. This results in a discrete consistency between the N(non-LTE) and the N(LTE). nevertheless, an important advantage of non-LTE analysis is that it allows to constrain the gas density, thus providing a means to validate the previous modelling predictions.

Still, in view of future observation of the PO$^+$ ion in different sources, it is interesting to explore a wider range of densities and kinetic temperatures. To this aim, we present in Fig. 8 the trend of the T_{ex} of the $j = 1-0$ and $j = 2-1$ lines as function of $n(H_2)$ for three different values of T_{kin}. It can be seen that, for densities around 10^5 cm^{-3}, maser phenomena are predicted, because of an inversion of the population between the levels.

4 CONCLUSIONS

The present study was triggered by the recent detection of PO$^+$ in the ISM (Rivilla et al. 2022); its aim is to support the interpretation of the present and future observations of this ion by providing an accurate description of its collision with the main astrochemical perturber *para*-H_2. We characterized the interaction PES by computing over 3250 *ab initio* points using the CCSD(T)-F12a/aug-cc-pV(Q+d)Z level of theory in the four $\{R, \theta, \theta', \text{and } \phi\}$ Jacobi coordinates. Subsequently, we fitted the potential as an expansion over angular functions. Before performing scattering calculations, we assessed the coupling effects between the $j = 0$, 2 rotational states of H_2, which showed a minor impact on the cross-sections. This allowed us to significantly simplify the scattering calculations by employing a spherical approximation of the potential averaged over five different orientations of H_2. Also, the comparison of some values of the cross-sections between *para*-H_2 and *ortho*-H_2 revealed a good collisional agreement of the two species. This, as exhibited for other ions too (Kłos & Lique 2011; Walker et al. 2017; Dagdigian 2019; Desrousseaux et al. 2019; Lara-Moreno, Stoecklin & Halvick 2019), suggests that the obtained results with *para*-H_2 are adequate to describe the collisional behaviour of PO$^+$ even at high temperatures, where the influence of *ortho*-H_2 may also have an impact. The state-to-state collisional coefficients between the twenty lowest rotational

levels of PO^+ and for temperatures ranging from 5 to 200 K were thus derived. A comparison with the data recently obtained by Chahal & Dhilip Kumar (2023) for the PO^+ and He collisional system revealed large discrepancies in the rate coefficients values, up to one order of magnitude in several cases, even despite the mass scaled contribution. This proves, for astrophysical purposes, a scarce reliability of He to simulate the behaviour of H_2 as colliding perturber of PO^+.

Finally, the computed collisional dataset allowed us to refine the abundance of PO^+ measured in the G+0.693–0.027 cloud, which resulted quite consistent with the one derived with LTE approximation (only a factor of ~ 1.7 lower). Moreover, the derived H_2 density of the gas (1.5×10^4 cm^{-3}) resulted in good agreement with previous estimates (Zeng et al. 2020). Radiative transfer calculations revealed maser behaviour for the first rotational transitions of PO^+ at different T_{kin} for densities around 10^4-10^6 cm^{-3}. These conditions encompass a significant portion of the interstellar sources, thus foregrounding the importance of the computed collisional coefficients to ensure an accurate modelling of the abundance of PO^+ in the ISM.

ACKNOWLEDGEMENTS

This work has been supported by MUR (PRIN grant number 202082CE3T) and by the University of Bologna (RFO funds). The COST Action CA21101 'COSY – Confined molecular systems: from a new generation of materials to the stars' is also acknowledged. Moreover, we acknowledge financial support from the European Research Council (Consolidator Grant COLLEXISM, grant agreement number 811363). François Lique acknowledges financial support from the Institut Universitaire de France and the Programme National 'Physique et Chimie du Milieu Interstellaire' (PCMI) of CNRS/INSU with INC/INP cofunded by CEA and CNES. VMR acknowledges support from the project RYC2020-029387-I funded by MCIN/AEI/10.13039/501100011033.

DATA AVAILABILITY

The data underlying this article will be made available through the LAMDA (Schöier et al. 2010; van der Tak et al. 2020) and BASECOL (Dubernet et al. 2013) data bases.

REFERENCES

Adler T. B., Knizia G., Werner H.-J., 2007, J. Chem. Phys., 127, 221106
Agúndez M., Cernicharo J., Guélin M., 2007, ApJ, 662, L91
Agúndez M., Cernicharo J., Decin L., Encrenaz P., Teyssier D., 2014, ApJL, 790, L27
Alessandrini S., Tonolo F., Puzzarini C., 2021, J. Chem. Phys., 154, 054306
Alexander M. H., 1984, J. Chem. Phys., 81, 4510
Alexander M. H., Manolopoulos D. E., 1987, J. Chem. Phys., 86, 2044
Altwegg K. et al., 2016, Sci. Adv., 2, e1600285
Balança C., Scribano Y., Loreau J., Lique F., Feautrier N., 2020, MNRAS, 495, 2524
Baptista L., De Almeida A. A., 2023, J. Phys. Chem. A, 127, 1000
Bergner J. B., Öberg K. I., Walker S., Guzmán V. V., Rice T. S., Bergin E. A., 2019, ApJL, 884, L36
Bergner J. B. et al., 2022, Front. Astron. Space Sci., 8, 246
Bop C. T., 2019, MNRAS, 487, 5685
Boys S. F., Bernardi F., 1970, Mol. Phys., 19, 553
Bregman J., Lester D., Rank D., 1975, ApJ, 202, L55
Brown J. M., Brown J. M., Carrington A., 2003, Rotational Spectroscopy of Diatomic Molecules. Cambridge Univ. Press, Cambridge
Cabrera-González L., Páez-Hernández D., Denis-Alpizar O., 2020, MNRAS, 494, 129
Chahal P., Dhilip Kumar T., 2023, MNRAS, 523, 5869
Chantzos J., Rivilla V. M., Vasyunin A., Redaelli E., Bizzocchi L., Fontani F., Caselli P., 2020, A&A, 633, A54
Colzi L. et al., 2022, ApJL, 926, L22
de la Concepción J. G., Puzzarini C., Barone V., Jiménez-Serra I., Roncero O., 2021, ApJ, 922, 169
Dagdigian P. J., 2019, J. Chem. Phys., 150, 084308
Denis-Alpizar O., Rubayo-Soneira J., 2019, MNRAS, 486, 1255
Desrousseaux B., Quintas-Sánchez E., Dawes R., Lique F., 2019, J. Phys. Chem. A, 123, 9637
Dubernet M.-L. et al., 2013, A&A, 553, A50
Dunning T. H., Jr, Peterson K. A., Wilson A. K., 2001, J. Chem. Phys., 114, 9244
Edmonds A. R., 2016, Angular Momentum in Quantum Mechanics. Princeton Univ. Press, Princeton
Fagerbakke K. M., Heldal M., Norland S., 1996, Aquat. Microb. Ecol., 10, 15
Fontani F., Rivilla V., Caselli P., Vasyunin A., Palau A., 2016, ApJL, 822, L30
Goldsmith P. F., Langer W. D., 1999, ApJ, 517, 209
Green S., 1975, J. Chem. Phys., 62, 2271
Guélin M., Cernicharo J., Paubert G., Turner B., 1990, A&A, 230, L9
Halfen D., Clouthier D., Ziurys L. M., 2008, ApJ, 677, L101
Huber K., Herzberg G., Huber K., Herzberg G., 1979, Molecular Spectra and Molecular Structure: IV. Constants of Diatomic Molecules. Springer, New York, p. 1
Hutson J. M., Green S., 1994, MOLSCAT version 14. Distributed by Collaborative Computational Project No. 6. Engineering and Physical Sciences Research Council, Swindon
Jankowski P., Szalewicz K., 1998, J. Chem. Phys., 108, 3554
Jiménez-Serra I., Viti S., Quénard D., Holdship J., 2018, ApJ, 862, 128
Kendall R. A., Dunning T. H., Jr, Harrison R. J., 1992, J. Chem. Phys., 96, 6796
Kłos J., Lique F., 2011, MNRAS, 418, 271
Knizia G., Adler T. B., Werner H.-J., 2009, J. Chem. Phys., 130, 054104
Lara-Moreno M., Stoecklin T., Halvick P., 2019, MNRAS, 486, 414
Lebouteiller V., Ferlet R., 2005, A&A, 443, 509
Lefloch B. et al., 2016, MNRAS, 462, 3937
Lique F., Faure A., 2019, Gas-Phase Chemistry in Space; From Elementary Particles to Complex Organic Molecules, Institute of Physics Publishing, Bristol
Manolopoulos D., 1986, J. Chem. Phys., 85, 6425
Öberg K. I., Bergin E. A., 2021, Phys. Rep., 893, 1
Pasek M. A., Lauretta D. S., 2005, Astrobiology, 5, 515
Pearce B. K., Pudritz R. E., Semenov D. A., Henning T. K., 2017, Proc. Natl. Acad. Sci., 114, 11327
Peterson K. A., Adler T. B., Werner H.-J., 2008, J. Chem. Phys., 128, 084102
Petrmichl R. H., Peterson K. A., Woods R. C., 1991, J. Chem. Phys., 94, 3504
Postberg F. et al., 2023, Nature, 618, 489
Raghavachari K., Trucks G. W., Pople J. A., Head-Gordon M., 1989, Chem. Phys. Lett., 157, 479
Ridgway S. T., Wallace L., Smith G. R., 1976, ApJ, 207, 1002
Rivilla V., Fontani F., Beltrán M., Vasyunin A., Caselli P., Martín-Pintado J., Cesaroni R., 2016, ApJ, 826, 161
Rivilla V. et al., 2018, MNRASL, 475, L30
Rivilla V. M. et al., 2020, MNRAS, 492, 1180
Rivilla V. M. et al., 2022, Front. Astron. Space Sci., 9, 829288
Roueff E., Lique F., 2013, Chem. Rev., 113, 8906
Schöier F. L., van der Tak F. F., van Dishoeck E. F., Black J. H., 2005, A&A, 432, 369
Schöier F., van der Tak F., van Dishoeck E., Black J., 2010, Astrophysics Source Code Library, record ascl:1010
Schwartz A. W., 2006, Philos. Trans. R. Soc. B Biol. Sci., 361, 1743
Spielfiedel A., Senent M. L., Kalugina Y., Scribano Y., Balança C., Lique F., Feautrier N., 2015, J. Chem. Phys., 143
Stoecklin T., Denis-Alpizar O., Halvick P., Dubernet M.-L., 2013, J. Chem. Phys., 139, 034304

Van der Tak F., Black J. H., Schöier F., Jansen D., van Dishoeck E. F., 2007, A&A, 468, 627
van der Tak F. F., Lique F., Faure A., Black J. H., van Dishoeck E. F., 2020, Atoms, 8, 15
Tenenbaum E., Woolf N., Ziurys L. M., 2007, ApJ, 666, L29
Tonolo F., Bizzocchi L., Melosso M., Lique F., Dore L., Barone V., Puzzarini C., 2021, J. Chem. Phys., 155, 234306
Tonolo F., Lique F., Melosso M., Puzzarini C., Bizzocchi L., 2022, MNRAS, 516, 2653
Turner B., Bally J., 1987, ApJ, 321, L75
Viana R. B., Pereira P. S., Macedo L. G., Pimentel A. S., 2009, Chem. Phys., 363, 49
Walker K. M., Lique F., Dumouchel F., Dawes R., 2017, MNRAS, 466, 831
Werner H. J., Knowles P. J., Knizia G., Manby F. R., Schütz M., 2012, WIREs Comput. Mol. Sci., 2, 242
Wernli M., 2006, PhD thesis, Univ. Joseph Fourier
Wernli M., Wiesenfeld L., Faure A., Valiron P., 2007a, A&A, 464, 1147
Wernli M., Wiesenfeld L., Faure A., Valiron P., 2007b, A&A, 475, 391
Woon D. E., Dunning T. H., Jr, 1993, J. Chem. Phys., 98, 1358
Yazidi O., Ben Abdallah D., Lique F., 2014, MNRAS, 441, 664
Zeng S. et al., 2018, MNRAS, 478, 2962
Zeng S. et al., 2020, MNRAS, 497, 4896
Ziurys L. M., 1987, ApJ, 321, L81

This paper has been typeset from a TEX/LATEX file prepared by the author.